Magnetic Resonance Imaging 74 (2020) 64–73

Contents lists available at ScienceDirect

Magnetic Resonance Imaging

journal homepage: www.elsevier.com/locate/mri

Original Contribution

Lung MRI assessment with high-frequency noninvasive ventilation at 3 T

Emeline Darçot[a,1], Jean Delacoste[a,1], Vincent Dunet[a], Gael Dournes[b,c,d], David Rotzinger[a], Maurizio Bernasconi[e,f], Petrut Vremaroiu[g], Julien Simons[h], Olivier Long[h], Chantal Rohner[a], Jean-Baptiste Ledoux[a,i], Matthias Stuber[a,i], Alban Lovis[f,1], Catherine Beigelman-Aubry[a,*,1]

[a] Department of Radiology, University Hospital (CHUV) and University of Lausanne (UNIL), Lausanne, Switzerland
[b] Univ. Bordeaux, Centre de Recherche Cardio-Thoracique de Bordeaux, U1045, CIC 1401, F-33000 Bordeaux, France
[c] Inserm, Centre de Recherche Cardio-Thoracique de Bordeaux, U1045, CIC 1401, F-33000 Bordeaux, France
[d] CHU de Bordeaux, Service d'Imagerie Thoracique et Cardiovasculaire, Service des Maladies Respiratoires, Service d'Exploration Fonctionnelle Respiratoire, CIC 1401, F-33600 Pessac, France
[e] Pulmonology, Department of Internal Medicine, Ospedale San Giovanni di Bellinzona, Bellinzona, Switzerland
[f] Department of Pulmonology, University Hospital (CHUV) and University of Lausanne (UNIL), Lausanne, Switzerland
[g] Centre d'investigation et de Recherche sur le Sommeil (CIRS), Lausanne, Switzerland
[h] Department of Physiotherapy, CHUV and University of Lausanne, Lausanne, Switzerland
[i] Center for Biomedical Imaging (CIBM), Lausanne, Switzerland

ARTICLE INFO

Keywords:
UTE
Respiratory stabilization
Lung
High-frequency ventilation
3 T

ABSTRACT

Purpose: To investigate three MR pulse sequences under high-frequency noninvasive ventilation (HF-NIV) at 3 T and determine which one is better-suited to visualize the lung parenchyma.

Methods: A 3D ultra-short echo time stack-of spirals Volumetric Interpolated Breath-hold Examination (UTE Spiral VIBE), without and with prospective gating, and a 3D double-echo UTE sequence with spiral phyllotaxis trajectory (3D radial UTE) were performed at 3 T in ten healthy volunteers under HF-NIV. Three experienced radiologists evaluated visibility and sharpness of normal anatomical structures, artifacts assessment, and signal and contrast ratio computation. The median of the three readers'scores was used for comparison, $p < .05$ was considered statistically significant. Incidental findings were recorded and reported.

Results: The 3D radial UTE resulted in less artifacts than the non-gated and gated UTE Spiral VIBE in inferior (score $_{\text{3D radial UTE}} = 3$, slight artifact without blurring vs. score $_{\text{UTE Spiral VIBE non-gated and gated}} = 2$, moderate artifact with blurring of anatomical structure, $p = .018$ and $p = .047$, respectively) and superior lung regions (score $_{\text{3D radial UTE}} = 3$, vs. score $_{\text{UTE Spiral VIBE non-gated}} = 2.5$, $p = .48$ and score $_{\text{UTE Spiral VIBE gated}} = 1$, severe artifact with no normal structure recognizable, $p = .014$), and higher signal and contrast ratios ($p = .002$, $p = .093$). UTE Spiral VIBE sequences provided higher peripheral vasculature visibility than the 3D radial UTE (94.4% vs 80.6%, respectively, $p < .001$). The HF-NIV was well tolerated by healthy volunteers who reported on average minor discomfort. In three volunteers, 12 of 18 nodules confirmed with low-dose CT were identified with MRI (average size 2.6 ± 1.2 mm).

Conclusion: The 3D radial UTE provided higher image quality than the UTE Spiral VIBE. Nevertheless, a better nodule assessment was noticed with the UTE Spiral VIBE that might be due to better peripheral vasculature visibility, and requires confirmation in a larger cohort.

1. Introduction

Interest in lung MRI has recently increased and despite the main challenges that include the low proton density of the lung tissue and the rapid signal dephasing due to sharp variations in magnetic susceptibility at the multiple tissue-air interfaces present in the lung, it is gradually translating into clinical use due to the multiple MR sequences available. The most common recommended MR sequences for pulmonary MRI are T_1- and T_2-weighted fast spin echo (FSE) as well as T_1-weighted 3D gradient-echo (GRE) volumetric interpolated breath-

* Corresponding author at: Department of Radiology, Centre Hospitalier Universitaire Vaudois (CHUV), Rue du Bugnon 46, BH 09 074, 1011 Lausanne, Switzerland.
E-mail address: catherine.beigelman-aubry@chuv.ch (C. Beigelman-Aubry).
[1] Both authors contributed equally to this work.

https://doi.org/10.1016/j.mri.2020.09.006
Received 17 February 2020; Received in revised form 12 August 2020; Accepted 2 September 2020
Available online 06 September 2020

hold examination (VIBE) before and after the injection of gadolinium-based contrast, T_2-weighted Half-Fourier Acquisition Single-shot Turbo spin Echo (HASTE), T_2-weighted BLADE and balanced steady state free precession (bSSFP) sequences. These sequences have the advantage of being easily available in medical centers and allow the investigation of a large panel of diseases that includes pneumonia [1,2], tuberculosis [3], cystic fibrosis [4], lung cancer [5] and the context of pulmonary nodules [6,7]. Among the most recent developments in lung MR to overcome the main challenges cited above, ultra-short echo time (UTE) imaging proved to be particularly suited to image the lung parenchyma and airways [8–12]. UTE has furthermore been investigated in the assessment of various pulmonary and airway disorders such as interstitial lung diseases, cystic fibrosis [10,13], and pulmonary nodule assessment [14].

Another major challenge of lung imaging is the respiratory motion that induces artifacts. One way to minimize respiratory motion is to perform breath-hold acquisitions. While breath-hold techniques have shown their efficiency [15,16], they result in time constraints and are challenging for patients with lung disease, who often suffer from a decreased lung function. Given that a successful breath-hold cannot be guaranteed and that non-compliant breath-holds result in images of poor quality with potential misregistration artifacts, free-breathing acquisitions with motion correction or motion-resolved techniques are now increasingly being investigated.

While breath-hold acquisitions are commonly performed at end-inspiration, free-breathing acquisitions are usually performed at tidal volumes. However, a well-known problem is that some lesions, such as those encountered in interstitial lung diseases, or lung nodules may be missed when lungs are not well inflated, particularly if located at the lung bases [17]. Therefore, a large lung volume is highly desired to provide an optimal and accurate diagnosis. Such optimal volumes are obtained routinely with computed tomography (CT), the gold standard technique in chest imaging, which is performed nowadays at end inspiration in less than 5 s for most chest studies. Several motion-correction strategies such as XD-UTE [18] and iMoCo UTE [19] have also been recently developed to improve free-breathing lung MRI, allowing for reduced respiratory motion artifacts and increased SNR. This study proposes a new strategy to ensure an optimal lung imaging volume while minimizing motion artifacts by using high-frequency noninvasive ventilation (HF-NIV). This technique allows an apnea-like stabilized ventilation of several minutes at full inspiration. Initially applied for radiotherapy [20], HF-NIV proved to be highly valuable for lung MRI [21]. Delacoste et al. recently demonstrated the superiority of the combination UTE-HF-NIV at 1.5 T [22] compared to acquisitions without the use of HF-NIV, such as free-breathing UTE [23] acquisition or breath-hold VIBE acquisition, a 3D gradient echo sequence used in clinical routine with an asymmetric sampling in the readout direction. A significant improvement in the sharpness of vessels and airways, lung-liver interface as well as in contrast and signal ratios was observed under HF-NIV. These results appeared potentially promising for the assessment of tiny details, such as small lung nodules as a better differentiation from vessels is expected. Among the UTE sequences dedicated to image the lung parenchyma, the 3D double-echo radial UTE sequence investigated by Delacoste et al. [22] as well as the 3D stack-of-spiral UTE sequence that allows prospective gating [10] appear promising.

Therefore, considering the superiority of MR-UTE-HF-NIV compared to free-breathing MR acquisitions, the goal of the study was to compare three acquisition techniques based on the two above-mentioned pulse sequences and to determine whether an acquisition technique is better-suited than another for the analysis of the lung parenchyma under HF-NIV at 3 T.

2. Material and methods

Permission from the ethics committee (CER-VD) was secured for this prospective study, for clinic and research exams (Project-ID 2018-00438). All volunteers provided written specific informed consent prior to the MR procedure. In case of incidental findings that required an additional CT exam for the incidental findings care, the volunteers in question provided either oral specific informed consent and/or written general informed consent.

2.1. Healthy volunteers

Ten healthy volunteers were recruited for the study (mean age 27 ± 5 years, mean weight 74 ± 10 kg, two women). To be included in the study, volunteers had to be in good health, age ≥18 years. Prior to MRI, volunteers underwent a HF-NIV training session to evaluate their tolerance to the HF-NIV and to maximize compliance during the MR exam.

2.2. HF-NIV

The HF-NIV set up is the same as that described by Delacoste et al. at 1.5 T [24], and consists of a Monsoon III ventilator (Acutronic Medical Systems, Hirzel, Switzerland) and a noninvasive patient interface (Oral mask, Oracle – Fisher&Paykel Healthcare, Auckland, New Zealand combined to Phasitron®, Percussionnaire, Idaho, USA) [21]. The stabilization period was achieved at a frequency rate of 250 per minute in agreement with findings reported by Ogna et al. [25]. The oxygen delivery has been set to 100% at the monitor (Fig. 1). In practice, given the ingress of ambient air through the inspiratory port of the Phasitron®, the fraction of inspired oxygen (FiO_2) was ~50%. The

Fig. 1. Training session. A respiratory physiotherapist trains a volunteer on how to position himself and behave to perform the HF-NIV, which requires a monitor (1), a Phasitron® (2) and a nose clip (3). (References: Delacoste et al. (2019) Ultrashort echo time imaging of the lungs under high-frequency noninvasive ventilation: A new approach to lung imaging. J Magn Reson Imaging 50(6):1789–1797. Video: https://www.youtube.com/watch?v=I4fo2uM9E5E).

specificities for MRI were as described by Delacoste et al. [24].

Continuous transcutaneous capnography ($TcCO_2$) oxygen saturation (SpO_2) and cardiac frequency were assessed during the training ventilation sessions using a Digital Monitoring System (SenTec, Therwil, Switzerland), as well as the arterial pressure. Due to MR constraints only SpO_2 and cardiac frequency were controlled during the MRI sessions.

After the training session (Fig. 1) and the MR exam, volunteers were asked to evaluate their discomfort regarding the HF-NIV (0 = no discomfort, 1 = minor discomfort, 2 = moderate discomfort, 3 = high discomfort, 4 = extreme discomfort).

2.3. Image acquisition and reconstruction

All acquisitions were performed on a 3 T clinical MR scanner (MAGNETOM Prisma FIT, software version VE11C, Siemens Healthcare, Erlangen, Germany), equipped with an 18-element RF body coil and 32-element spine coil. Volunteers were in supine position, feet first. Three sequences were acquired under HF-NIV, during a respiratory stabilization period. A prototype 3D double-echo radial UTE sequence [23,26] with spiral phyllotaxis trajectory [27] was used to acquire data without any ECG nor respiratory triggering (referred to as "3D radial UTE", Table 1). Images were reconstructed in Matlab (The Mathworks, Natick, Massachusetts, USA) with a non-uniform fast Fourier transform.

Additionally, a 3D UTE stack-of spirals sequence [28,29] was acquired in the coronal plane without and with prospective respiratory gating (referred to as "UTE Spiral VIBE non-gated" and "UTE Spiral VIBE gated", respectively, Table 1). The respiratory gating was performed without navigator positioning but with the selection of a coil element close to the liver-diaphragm interface for signal processing, data were acquired in expiratory phase. The gating detected the respiratory signal in real time with a temporal resolution of 212 ms. Given that the motion period under HF-NIV was 240 ms, the gating should have been able to reduce artifacts from the residual motion under HF-NIV. Images from both UTE Spiral VIBE acquisitions were directly reconstructed at the scanner, while 3D radial UTE images were reconstructed off-line.

The three acquisitions under HF-NIV were separated by a rest period of a few minutes where patients resumed a normal breathing.

The three protocols were defined to be consistent in terms of spatial resolution and acquisition time.

2.4. Image analysis

Three experienced radiologists (GD and VD with 8 years and CB with more than 20 years of experience in thoracic imaging) analyzed anonymized datasets of the three investigated acquisitions. The experts were blinded to the acquisition method used for images and they graded and analyzed them in a random order, in axial orientation. The fissures were evaluated for right and left lungs through their visibility, scored as 1 = not visible; 2 = partially visible and 3 = completely visible, and their sharpness, evaluated as 1 = not seen; 2 = blurred; 3 = intermediate; 4 = sharp. The presence of artifacts either in superior, medium, or inferior parts of the lungs were scored for right and left lungs as follows: 1 = severe artifact with no normal structure recognizable; 2 = moderate artifact with blurring of anatomical structures; 3 = slight artifact without blurring of anatomical structures; 4 = no artifact.

The visibility and sharpness of pulmonary vasculature and airways were evaluated in eighteen segments per volunteer with a distinction between the peripheral vasculature that corresponds to the external third of the chest and the central vasculature that corresponds to the two medial thirds of the chest. The scoring was performed according to a slightly modified version of that by Ohno and colleagues [13] for both central vasculature and airways visibility: 1 = no depiction; 2 = depicted at segmental level; 3 = depicted at subsegmental level; 4 = depicted at sub-subsegmental level; 5 = depicted beyond sub-subsegmental level. Peripheral vasculature visibility was scored as 1 = not visible; 2 = visible and was reported as a percentage of visibility for the whole chest. The sharpness of the central and peripheral vasculature and airways was scaled as follows: 1 = not seen; 2 = blurred; 3 = intermediate; 4 = sharp.

To quantitatively assess the lung signal intensity (SI), regions of interest (ROIs) were manually drawn in eighteen different places [8]. The SI within air (SI_{airway}) was calculated as the average SI from ROIs drawn in the trachea and the right and left main bronchus. The SI within vessels (SI_{vessel}) was calculated as the average SI from ROIs traced in the pulmonary trunk and the right and left main pulmonary arteries. Finally, the SI within the lung parenchyma (SI_{lung}) was calculated as the average SI from 12 ROIs as follows: Each lung was divided in three axial sections at the level of the aortic arch, of the carina, and of the lower pulmonary veins. ROIs were placed at each location in the anterior and posterior part for both the right and left lungs, and at least 2 cm from the lung periphery avoiding vessels as much as possible. The signal ratio and contrast ratio were then calculated as follows [8,30]:

$$S_r = \frac{SI_{lung}}{SI_{airway}} \times 100 \quad (1)$$

$$C_r = \frac{SI_{lung} - SI_{airway}}{SI_{vessel}} \times 100 \quad (2)$$

The apex-dome distance was also measured in centimeters on a coronal plane on the right side.

Table 1
Acquisition parameters.

	UTE spiral VIBE non-gated	UTE spiral VIBE gated	3D radial UTE
Field of view (mm)	352 × 352	352 × 352	250 × 250 × 250
Voxel size (mm^3)	1	1	1
Slice number	256	224	–
TE_1/TE_2 (ms)	0.05/–	0.05/–	0.08/2.86
TR (ms)	3.7	3.53	5.9
Acquisition orientation	Coronal	Coronal	Transverse
Bandwidth BW_1/BW_2 (Hz/pixel)	945/–	980/–	305/610
RF excitation angle (°)	5	5	5
Spiral interleaves	380	236	–
Segments × readouts	–	–	1220 × 50
Slice partial Fourier	–	6/8	–
Acquisition time (min:s)	06:20	~06:00	06:00

2.5. Incidental findings

Any incidental finding was recorded and subsequently evaluated with an ultra-low-dose CT if judged as potentially requiring subsequent management. The CT exams were performed on a SOMATOM Force scanner (Siemens Healthcare, Erlangen, Germany) without contrast administration, with a CT dose index (CTDI) between 0.35 and 0.5 mGy corresponding to an effective dose between 0.2 and 0.4 mSv, using a conversion factor of 0.017. The size and morphological characteristics of the findings among which the majority corresponded to lung nodules were assessed to determine if they were actionable or not according to current guidelines [31–33].

The number, location, and size of these findings were evaluated in MR images with the three investigated sequences, blinded and presented in a random order to two radiologists (CB, Reader 1, > 20 years of experience in thoracic imaging, and DR, Reader 2, 8 years of experience) more than eight months after the initial analyses and more

than two months after the clinical evaluation, which helped minimize recall bias. Only the images from the volunteers with incidental findings were included in this sub-study and these were analyzed in the same conditions as in clinical practice by using maximum intensity projection (MIP) post-processing, in an axial view. If needed, multiplanar reformats were used to confirm the presence of pulmonary nodules. In a subsequent review session, both readers analyzed CT images and associated corresponding findings with MR images in consensus. The detection rate per reader, per sequence and per volunteer was then calculated with the following formula:

$$Detection\ rate = \frac{True\ positive}{True\ positive + false\ negative} = \frac{True\ positive}{Gold\ standard\ positive} \quad (3)$$

2.6. Statistical analysis

Statistical analysis was carried out using R version 3.4.3 with the ggpubr package version 0.2. The inter-rater reliability was assessed with a Gwet's AC1 test for categorical variables. The observed agreement, AC1 score, and standard error were reported. The Landis and Koch scale was used to interpret the Gwet's AC1 coefficient as follows: poor when Gwet's AC1 was < 0.00, slight between 0.01 and 0.20, fair between 0.21 and 0.40, moderate between 0.41 and 0.60, substantial between 0.61 and 0.80 and excellent above 0.81. The tests were assessed for each item and each method: UTE Spiral VIBE non-gated, gated, and 3D radial UTE sequences. Depending on the item, either scores from the right and left lungs were combined or all segments were combined.

The median of the three observers' scores was used to compare the three methods and a Kruskal-Wallis test by ranks was used to evaluate the visual scores. When this test revealed a significant difference, a pairwise comparison was performed using a Wilcoxon signed-rank test with Holm's correction for multiple comparisons. For the analysis of continuous variables, the average of the three observers' scores was used and an ANOVA test was carried out. A Student's paired t-test was performed with Holm's correction for pairwise comparison when necessary. P-values lower than 0.05 were considered statistically significant.

3. Results

3.1. Technical feasibility and tolerance

Volunteers' n°6 and n°8 were excluded from analysis as the 3D radial UTE and UTE Spiral VIBE gated images, respectively, were not interpretable due to software malfunctions not related to the HF-NIV technique. The analyses were therefore performed with 8 subject data.

The HF-NIV technique was well tolerated by all healthy volunteers who reported only a minor discomfort on average (average score = 1.4 ± 0.8, Min-max range [0–3]).

3.2. Inter-rater reliability

The inter-rater reliability of the fissure and artifacts evaluation showed either substantial or excellent agreement between the three readers (all AC1 scores > 0.61, p < .05), with the exceptions of the inferior artifacts evaluation with the UTE Spiral VIBE gated (AC1 = 0.52), the superior artifacts evaluation with 3D radial UTE (AC1 = 0.52) and the fissure visibility evaluation with UTE Spiral VIBE non-gated (AC1 = 0.40, Table 2).

The inter-rater reliability of the airway visibility and the central vasculature visibility were excellent for all methods. The inter-rater reliability of the peripheral vasculature visibility was excellent for the UTE Spiral VIBE non-gated and substantial for both UTE Spiral VIBE gated and 3D radial UTE (Table 3). While the AC1 score of both airway

Table 2
Inter-rater reliability of the fissure and artifacts scoring for the three evaluated methods.

	Artifacts Inf (1–4)			Artifacts Moy (1–4)			Artifacts Sup (1–4)			Fissure sharpness (1–4)			Fissure visibility (1–3)		
	AC1 score	Observed agreement	Standard error	AC1 score	Observed agreement	Standard error	AC1 score	Observed agreement	Standard error	AC1 score	Observed agreement	Standard error	AC1 score	Observed agreement	Standard error
UTE Spiral VIBE non-gated	0.79	0.88	0.10	0.65	0.83	0.07	0.76	0.91	0.08	0.69	0.84	0.13	0.40	0.67	0.18
UTE Spiral VIBE gated	0.52	0.80	0.09	0.65	0.82	0.10	0.79	0.92	0.07	0.95	0.96	0.04	0.91	0.92	0.07
3D radial UTE	0.89	0.94	0.05	0.73	0.85	0.11	0.52	0.75	0.16	0.92	0.93	0.06	0.91	0.92	0.07

All Gwet's AC1 scores had significant p-values (p < .05).

Table 3
Inter-rater reliability of the visibility scoring for the three evaluated methods.

	Airway visibility (1–5)			Central vasculature visibility (1–5)			Peripheral vasculature visibility (1–2)		
	AC1 score	Observed agreement	Standard error	AC1 score	Observed agreement	Standard error	AC1 score	Observed agreement	Standard error
UTE Spiral VIBE non-gated	0.84	0.94	0.01	0.96	0.96	0.01	0.87	0.88	0.03
UTE Spiral VIBE gated	0.89	0.95	0.01	0.96	0.96	0.01	0.75	0.80	0.04
3D radial UTE	0.85	0.95	0.02	0.96	0.96	0.01	0.61	0.73	0.05

All scores were significant ($p < .05$).

Table 4
Inter-rater reliability of the sharpness scoring for the three evaluated methods.

	Airway sharpness (1–4)			Central vessel sharpness (1–4)			Peripheral vessel sharpness (1–4)		
	AC1 score	Observed agreement	Standard error	AC1 score	Observed agreement	Standard error	AC1 score	Observed agreement	Standard error
UTE Spiral VIBE non-gated	0.92	0.95	0.01	0.87	0.94	0.02	0.86	0.93	0.02
UTE Spiral VIBE gated	0.91	0.95	0.01	0.71	0.89	0.03	0.48	0.81	0.05
3D radial UTE	0.75	0.90	0.03	0.72	0.90	0.03	0.29	0.77	0.06

All scores were significant ($p < .05$).

sharpness and central vasculature sharpness showed either substantial or excellent inter-rater reliability, peripheral vasculature sharpness scores showed slight and moderate inter-rater reliability for 3D radial UTE and UTE Spiral VIBE gated methods, respectively (Table 4).

3.3. Visual assessment

The visual assessment of the fissure sharpness and visibility revealed no significant difference between the three evaluated methods, with all median scores equal to 1, i.e. not visible. The visual assessment of the artifacts revealed a significantly higher median score in 3D radial UTE images compared to UTE Spiral VIBE non-gated and gated methods when scoring the inferior part of the lungs ($p = .018$ and $p = .047$, respectively, Fig. 2a). This was observed as well for the upper part of the lung, where a significant difference was observed between 3D radial UTE and UTE Spiral VIBE gated scores (score = 3 vs 1, $p = .014$, Fig. 2c), while no significant difference was observed when comparing 3D radial UTE to the UTE Spiral VIBE non-gated ($p = .48$) or when comparing both UTE Spiral VIBE methods with each other ($p = .1$). No significant differences were observed in the middle part of the lung (Fig. 2b).

The airway and central vasculature visibility were not significantly different among the images of the three analyzed methods. These features were depicted for all methods at subsegmental level and beyond sub-subsegmental level, respectively (Fig. 2d and e, Figs. 3 and 4). In images from both UTE Spiral VIBE sequences, the peripheral vasculature yielded a higher percentage of visibility than in images from the 3D radial UTE sequence ($p < .001$, Fig. 2f).

The evaluation of the airways and vasculature sharpness resulted in the same median score among the three methods (Fig. 5). Nevertheless, while no significant difference was observed among the three methods for the peripheral vasculature sharpness, for airway and central vasculature sharpness, the distributions on the scale from blurred to sharp were significantly different (Fig. 5).

The apex-dome distance measurements were non-significantly different in the images of the three different methods ($dist_{(UTE\ Spiral\ VIBE\ non\text{-}gated)} = 23.3 \pm 1.7$ cm; $dist_{(UTE\ Spiral\ VIBE\ gated)} = 23.0 \pm 2.1$ cm; $dist_{(3D\ radial\ UTE)} = 23.4 \pm 2.1$ cm, $p = .93$).

3.4. Signal intensity measurements

The 3D radial UTE images yielded significantly higher Sr than that measured from UTE Spiral VIBE non-gated and gated images by 2.1-fold and 1.9-fold, respectively ($p < .003$, Fig. 6). The Cr was higher in 3D radial UTE images than in UTE Spiral VIBE images ($p = .093$).

3.5. Incidental findings

Nodules and linear densities were incidentally detected in three of the healthy volunteers (Fig. 7) and the controlled CT exams detected 26 findings in total including 18 nodules (spread as 6-10-2 among the three volunteers) and 8 linear densities (3-2-3). Among these 18 nodules, 12 were detected with MRI by any reader or MR sequence. The average nodule size measured with CT was 2.6 ± 1.2 mm, including 5 nodules with a size ≥4 mm.

While Reader 2 analysis resulted in no difference in detection rate between the three sequences (39% for all nodules, 80% for nodules ≥4 mm), the 3D radial UTE sequence yielded the lowest detection rate in the analysis of Reader 1, such as 60% vs 80% for both UTE Spiral VIBE sequences and for nodules ≥4 mm (Table 5). This was due to a nodule that had a much lower contrast in the 3D radial UTE images than in both UTE spiral VIBE images (Fig. 7e–h). The linear densities were not evaluated in this analysis.

4. Discussion

Lung MRI has seen numerous developments to overcome the major drawbacks that include artifacts, lack of spatial resolution and lack of signal from the lungs due to the physical characteristics of this organ, and that have thus far prevented this non-invasive and safe technique to be used more widespread clinically. One of the most recent development is the UTE sequence that addresses these problems and that has proven to be suitable to image the lung parenchyma [11]. Moving forward toward improvement of lung imaging, the interest for chest MRI under the use of the HF-NIV technique has been recently emphasized by showing an increase in image quality when using a 3D radial UTE sequence with HF-NIV, compared to the same sequence without the ventilation technique at 1.5 T. To evaluate the potential of HF-NIV

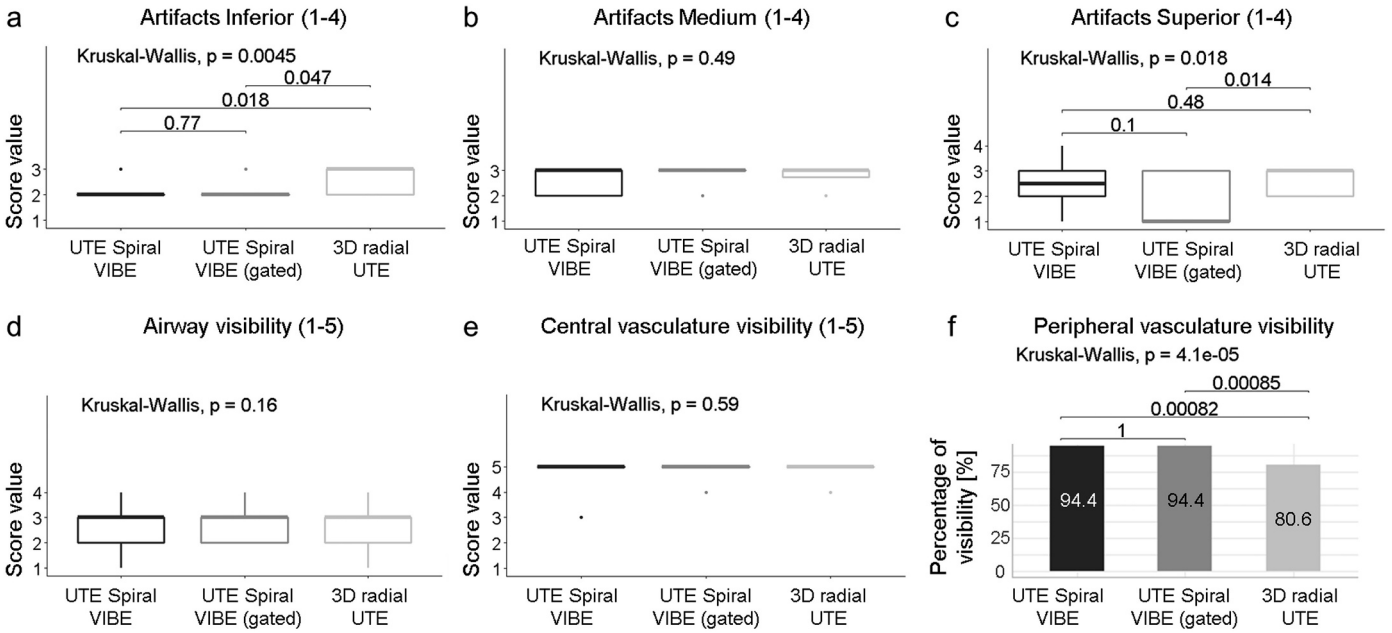

Fig. 2. Visual evaluation of artifacts, vasculature and airways visibility. The artifacts inferior a., medium b., superior c., the airways visibility d., the central vasculature e. and the peripheral vasculature visibility f., were evaluated for the three sequences and compared with the median of the three readers. The peripheral vasculature visibility was interpreted as percentage of visibility. The 3D radial UTE resulted in the highest score for the whole lung artifact evaluation with a median at 3, qualifying slight artifact without blurring of anatomical structures. While there was no significant difference between the sequences for airway and central vasculature visibility, a lower percentage of visibility was observed in peripheral vasculature with the 3D radial UTE sequence compared to both UTE Spiral VIBE sequences.

at 3 T, a comparison between three different acquisition methods for lung imaging with HF-NIV was performed and resulted in the superiority of the 3D radial UTE sequence when assessing the overall quality of the images, artifacts evaluation and Sr and Cr ratios.

The lower score in artifacts assessment for the UTE Spiral VIBE for the lower and upper parts of the lungs might be partially explained by the set-up of the MR exam. Indeed, due to the HF-NIV setup, patients are feet first in the MR scanner and the apex of the lungs, depending on the body size, could be at the limit of the spine coil. Besides, the FOV that was defined according to time and spatial resolution constraints, might have been a culprit factor and induced fold-over artifacts.

The visibility of the airways and central vasculature was similar for all three sequences, while the peripheral vasculature visibility was significantly lower in images acquired with the 3D radial UTE sequence, which cannot fully be explained but as a consequence, might be responsible for a lower detection of peripheral lesions such as the nodule located on the periphery of the left lung that had been considered as non-relevant by Reader 1 on the 3D radial UTE images. In light of the similarity of vasculature and airway sharpness with all three acquisition methods under HF-NIV, and taking into account that sharpness was significantly improved with the 3D radial UTE sequence under HF-NIV compared to 3D radial UTE sequence without HF-NIV in the 1.5 T study [24], this increased sharpness can be reasonably related to the ventilation technique rather than the sequence by itself.

Significantly higher Sr and Cr were reported in 3D radial UTE images than in UTE Spiral VIBE images. As mentioned by Dournes et al. [10], which compared the UTE Spiral VIBE to the PETRA sequence [8,34] and reported similar findings, these differences can be explained,

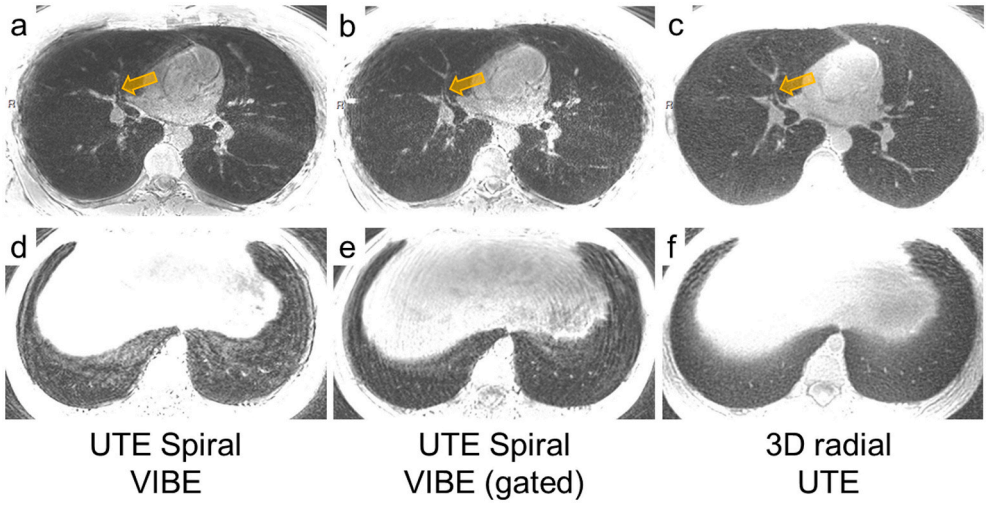

Fig. 3. Axial view 1 mm thick at the level of the subsegmental bronchi of the right middle lobe and at the lung bases. a-c. Images acquired with the UTE Spiral VIBE non-gated a., gated b. and with the 3D radial UTE c. sequences. An excellent assessment of the visibility of the subsegmental bronchi of the right middle lobe with less artifacts, which may potentially penalize the overall interpretation, can be observed in c. compared to a and b, (orange arrows). d-f. Lung base images acquired with the UTE Spiral VIBE without gating d., with gating e. and 3D radial UTE f. sequences. In addition to an excellent lung inflation volume, there is an improved image quality in c at the level of the lung bases, the first areas to be penalized in case of free-breathing or lack of full inspiration. Such an assessment may allow to optimize any lung abnormalities at this level that can be underestimated or missed in case of expiration.

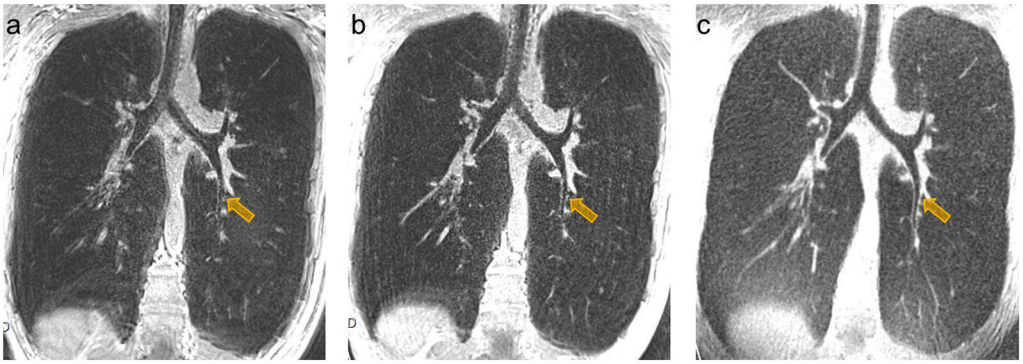

Fig. 4. Coronal oblique view 1 mm thick in the long axis of the proximal tracheobronchial tree. a. Image acquired with the UTE Spiral VIBE non-gated, b. gated and c. 3D radial UTE sequences. Note the better delineation of the walls of the posterobasal segmental bronchus of the left lower lobe in c (orange arrows). Regarding UTE Spiral VIBE images, note the undeniable reduction of artifacts in b that was acquired with the gated sequence compared to that of the non-gated sequence a.

at least partially, by the way the coverage of k-space was obtained. Indeed, the UTE Spiral VIBE uses a stack-of spirals to move from 2D to 3D while the PETRA sequence uses a radial spherical coverage of k-space, close to the spherical coverage of k-space with spiral phyllotaxis trajectory used with the 3D radial UTE in this study. Given that volunteers were not breathing room air but an oxygen-enriched air, the reported Sr and Cr might have been biased. Indeed, since O_2 is paramagnetic, the dissolved molecular oxygen induces a shortening of the T_1 relaxation time in the pulmonary venous blood and results in a SI increase in the lung parenchyma [35]. Nevertheless, the same FiO_2 was administered for all acquisitions, so no bias were introduced in the comparison of the MR sequences.

These high Sr and Cr along with the acquisition at full inspiration could therefore benefit a wide range of diseases, including the assessment of interstitial lung diseases (ILD), airway diseases and abnormal bronchi until subsegmental level. MRI has increasingly been investigating ILD [36]. In particular, since Ohno et al. [13] reported a non-significant inferiority of MRI with UTE compared with standard and low dose CTs regarding pulmonary parenchyma diseases and identification of ILD, the combination of MRI and HF-NIV might be of great additional interest. Indeed, underinflation of the lung may preclude a correct analysis of the subpleural and basal area, which may be disadvantageous in the assessment of major ILD and especially usual interstitial pneumonitis and non-specific interstitial pneumonitis. The same approach should also be considered with airway diseases, while it is gradually more investigated with MRI [23,37,38]. Nevertheless, excellent results are currently obtained and the benefit of HF-NIV might be less obvious than for ILD in this setting. The major challenge will then be to determine the precise exclusion criteria for patients with severe ILD or airway disease, knowing that the only formal contra-indications to HF-NIV are major hyperinflation and pulmonary hypertension. Indeed, if HF-NIV use is currently restricted among others to patients without COPD or asthma with severe obstruction - i.e. severe obstructive patients (FEV1 < 50% of predicted value), hypoxemia (SaO2 < 94% AA) – history or physical signs of right heart failure, and also to patients without history or physical signs of pulmonary hypertension, this has been designed as safety measure for the current investigation of the HF-NIV technique.

For pulmonary nodule assessment specifically, it could help to formally diagnose a juxta-vascular pulmonary nodule, considering that the tortuosity of vessels remains a critical challenge that may induce misleading interpretations, and to accurately measure pulmonary nodule's volume.

In this study, the nodules' detection are mentioned as preliminary data and while the 3D radial UTE sequence with HF-NIV appeared the most promising sequence that obtained the highest grades for image quality, it did not provide the highest detection rate, at least for one reader out of two. This result might be related to the lower peripheral vasculature visibility observed in 3D radial UTE images compared to UTE Spiral VIBE images. This must now be evaluated in a large cohort of patients with pulmonary nodules along with the UTE Spiral VIBE gated sequence. Compared to Rana et al. who reported 100% sensitivity for nodules > 4 mm, and 35% sensitivity for nodules < 4 mm [39], we found a lower detectability for nodules ≥ 4 mm and a rather similar detectability for nodules < 4 mm for the UTE Spiral VIBE gated sequence. These results have to be weighted by the small size and the low number of evaluated nodules, the majority of which were from two volunteers only, even though the image quality scores of these volunteers' images were within the range of the overall scores. Furthermore, the detection rate of all sequences remained within the range reported in literature [6,40,41]. Interestingly, although there is no need to detect nodules < 5 mm for screening programs according to the recent guidelines [32,33,42], assessment of smaller lesions may concern disorders such as ILD like sarcoidosis and such an evaluation has therefore all its place and interest.

MIPs were of interest for the assessment of nodule detection and could also be used in disorders such as micronodular pattern for example. Additional minimal intensity projection (mIP) post-processing should be further evaluated for ILD.

Finally, the question of the optimal magnetic field strength still remains for MR lung imaging. On the one hand, while Chassagnon et al. [43] who compared high-resolution MR lung imaging with the UTE

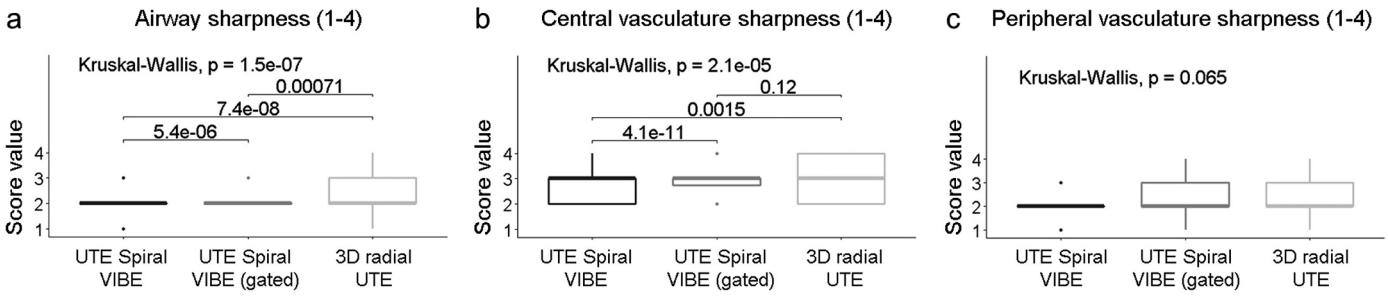

Fig. 5. Visual evaluation of vasculature and airways sharpness. The airway a., the central vasculature b. and the peripheral vasculature c. sharpness, were evaluated for the three sequences and compared with the median of the three readers. No significant difference was observed between the sequences that yielded the same median scores.

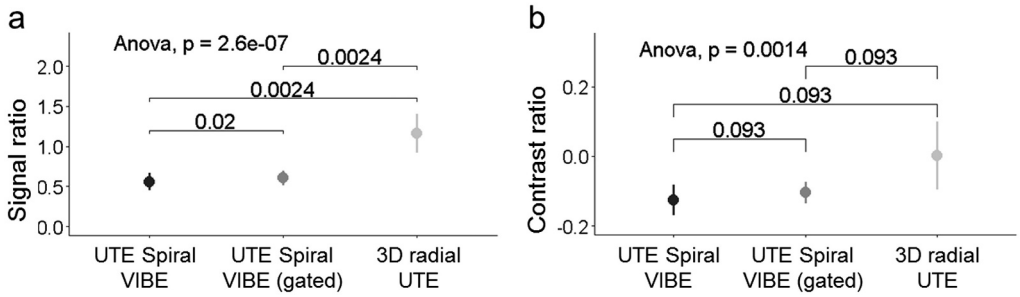

Fig. 6. Signal and contrast ratios quantification for the UTE Spiral VIBE non-gated, gated, and the 3D radial UTE sequences. The signal ratio a. and contrast ratio b. were calculated and the average of the three readers was used for comparison. Images acquired with 3D radial UTE resulted in significantly higher signal ratio compared to images acquired with both UTE Spiral VIBE sequences.

Spiral VIBE sequence at 1.5 T and 3 T, demonstrated that image quality was lower at 3 T than at 1.5 T, with significantly lower Sr and Cr reported at 3 T than at 1.5 T, more and more studies are performed at 3 T driven by the need for a higher spatial resolution in order to improve the precision and accuracy of nodule detection. On the other hand, Campbell-Washburn et al. recently demonstrated the value of the high-performance low-field-strength MRI at 0.55 T in high-susceptibility regions such as lungs [44]. The improved field-homogeneity at 0.55 T allowed an increase in signal intensity and a reduction of the distortion near air-tissue interfaces.

The main limitation of the HF-NIV-MRI combination is the medical requirements of the HF-NIV, such as the presence of a respiratory physiotherapist and a pulmonologist during the MRI acquisition, as well as the need for a training session prior to the MR procedure. In addition technical limitations related to a non-compatible MRI ventilator that requires a long pipe reducing ventilation efficiency should be solved. Therefore, although an undeniably added value of the HF-NIV was demonstrated in past and in the present MR study, the spread of the use of HF-NIV with MR lung imaging may be limited. For this reason, a simplification of the ventilation technique would be most welcome. The small sample size and the impracticability of volunteer recruitment at a distance from the main image quality analysis are also limitations of this study. Furthermore, the potential recognition of the different MR sequences might have induced a bias despite the anonymization and

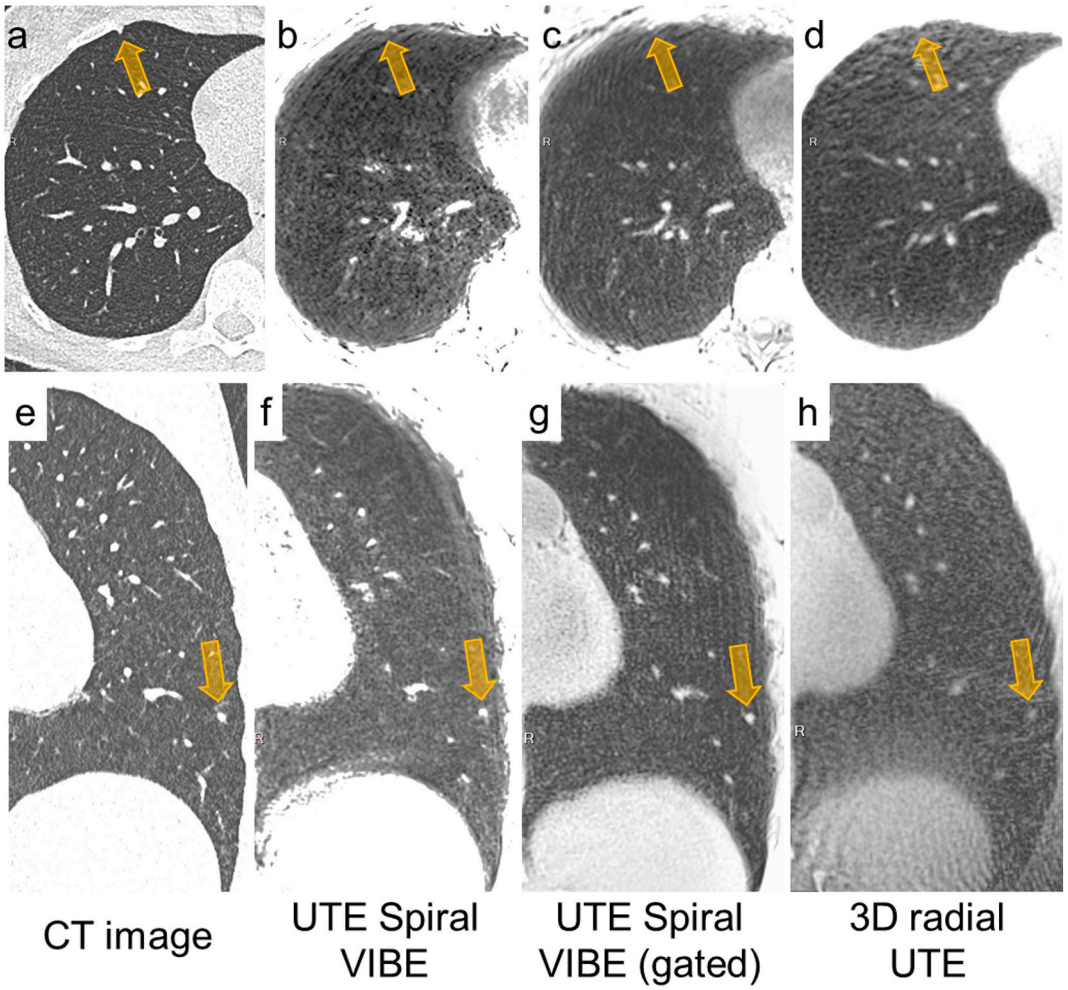

Fig. 7. Nodules observed in two healthy volunteers with CT and MR sequences. a-d. Axial view acquired with CT a., UTE Spiral VIBE non-gated b., gated c. and 3D radial UTE d. sequences. The nodule (orange arrows) was only seen and reported as such with CT. e-h. Coronal view acquired with CT e., UTE Spiral VIBE non-gated f., gated g. and 3D radial UTE h. sequences. Although visible with all MR sequences, the nodule (orange arrows) was much less visible on 3D radial UTE sequences due to the low contrast with the neighboring parenchyma and considered as non-relevant by one reader.

Table 5
Nodule detection rates in healthy volunteers with incidental findings.

		UTE spiral VIBE non-gated	UTE spiral VIBE gated	3D radial UTE
Reader 1	All nodules (n = 18)	44%	50%	33%
	Nodules ≥4 mm (n = 5)	80%	80%	60%
	Nodules < 4 mm (n = 13)	31%	38%	23%
Reader 2	All nodules (n = 18)	39%	39%	39%
	Nodules ≥4 mm (n = 5)	80%	80%	80%
	Nodules < 4 mm (n = 13)	23%	23%	23%

The average nodule size was 2.6 ± 1.2 mm, with 5 nodules ≥4 mm out of 18. While the analysis of Reader 2 resulted in equal detection rate for all sequences, the 3D radial UTE provided the lowest detection rate with Reader 1 results.

randomization of images during the image quality and the lung nodules assessment. Although the nodule detection analysis was performed as proof of principle considering the low number of volunteers, it includes several limitations: while anonymization was performed among the different sequences and volunteers, only datasets in which nodules had been discovered were analyzed. This might have induced a bias and prevented from calculating the specificity of each sequence. Furthermore, the delay between the MRI exam and the CT exam was sometimes of several months. Therefore while reducing the recall bias, this delay might also have induced a less reliable comparison between the two sets of images, with the potential removal or appearance of small lung nodules. Besides, the small size of the subgroup with incidental nodules precludes a definite assessment of the detection rate, therefore our results have to be confirmed in a larger cohort. Finally, the risk of recall bias was minimized even though not excluded along the whole study.

5. Conclusion

Among the three sequences performed under HF-NIV, the 3D radial UTE allows for a significant improvement of image quality compared to UTE Spiral VIBE non-gated and gated. The interesting potential of the UTE Spiral VIBE owing to the better peripheral vessel visibility remains to be explored. These results may therefore be promising as a step toward improved MR lung imaging. Among the potential advantages, the ability to replace or complement CT exams by MR for the follow up of lung nodules, especially thanks to the acquisition at full inspiration, appears to be very promising.

Declaration of Competing Interest

Non-monetary research support was provided by Siemens Healthineers to MS.

Acknowledgments

The UTE Spiral VIBE pulse sequence used in this study is a prototype research sequence provided by Siemens Healthcare. We would like to thank Mrs. Kathleen Grant for her assistance throughout the project and Professors Reto Meuli and John Prior for their support. We also thank the Center for Biomedical Imaging (CIBM) for its support. This work was supported by grants from the Swiss National Science Foundation to CB (n°320030_176241) and to MS (n°143923 and REQUIP n° 150828), and a scholarship from the Leenaards foundation, Switzerland (Bourse Relève 2017 Réf. 4890.0) to AL.

References

[1] Ekinci A, Yucel Ucarkus T, Okur A, Ozturk M, Dogan S. MRI of pneumonia in immunocompromised patients: comparison with CT. Diagn Interv Radiol 2017;23(1):22–8.
[2] Liszewski MC, Gorkem S, Sodhi KS, Lee EY. Lung magnetic resonance imaging for pneumonia in children. Pediatr Radiol 2017;47(11):1420–30.
[3] Zeng J, Liu Z, Shen G, Zhang Y, Li L, Wu Z, et al. MRI evaluation of pulmonary lesions and lung tissue changes induced by tuberculosis. Int J Infect Dis 2019;82:138–46.
[4] Wielputz MO, Eichinger M, Biederer J, Wege S, Stahl M, Sommerburg O, et al. Imaging of cystic fibrosis lung disease and clinical interpretation. Rofo 2016;188(9):834–45.
[5] Meier-Schroers M, Homsi R, Gieseke J, Schild HH, Thomas D. Lung cancer screening with MRI: evaluation of MRI for lung cancer screening by comparison of LDCT- and MRI-derived lung-RADS categories in the first two screening rounds. Eur Radiol 2019;29(2):898–905.
[6] Cieszanowski A, Lisowska A, Dabrowska M, Korczynski P, Zukowska M, Grudzinski IP, et al. MR imaging of pulmonary nodules: detection rate and accuracy of size estimation in comparison to computed tomography. PLoS One 2016;11(6):e0156272.
[7] Kurihara Y, Matsuoka S, Yamashiro T, Fujikawa A, Matsushita S, Yagihashi K, et al. MRI of pulmonary nodules. AJR Am J Roentgenol 2014;202(3):W210–6.
[8] Dournes G, Grodzki D, Macey J, Girodet PO, Fayon M, Chateil JF, et al. Quiet Submillimeter MR imaging of the lung is feasible with a PETRA sequence at 1.5 T. Radiology 2015;276(1):258–65.
[9] Johnson KM, Fain SB, Schiebler ML, Nagle S. Optimized 3D ultrashort echo time pulmonary MRI. Magn Reson Med 2013;70(5):1241–50.
[10] Dournes G, Yazbek J, Benhassen W, Benlala I, Blanchard E, Truchetet ME, et al. 3D ultrashort echo time MRI of the lung using stack-of-spirals and spherical k-space coverages: evaluation in healthy volunteers and parenchymal diseases. J Magn Reson Imaging 2018;48(6):1489–97.
[11] Wielputz MO, Triphan SMF, Ohno Y, Jobst BJ, Kauczor HU. Outracing lung signal decay – potential of Ultrashort Echo time MRI. Rofo 2019;191(5):415–23.
[12] Bergin CJ, Pauly JM, Macovski A. Lung parenchyma: projection reconstruction MR imaging. Radiology 1991;179(3):777–81.
[13] Ohno Y, Koyama H, Yoshikawa T, Seki S, Takenaka D, Yui M, et al. Pulmonary high-resolution ultrashort TE MR imaging: comparison with thin-section standard- and low-dose computed tomography for the assessment of pulmonary parenchyma diseases. J Magn Reson Imaging 2016;43(2):512–32.
[14] Cha MJ, Park HJ, Paek MY, Stemmer A, Lee ES, Park SB, et al. Free-breathing ultrashort echo time lung magnetic resonance imaging using stack-of-spirals acquisition: a feasibility study in oncology patients. Magn Reson Imaging 2018;51:137–43.
[15] Gai ND, Malayeri A, Agarwal H, Evers R, Bluemke D. Evaluation of optimized breath-hold and free-breathing 3D ultrashort echo time contrast agent-free MRI of the human lung. J Magn Reson Imaging 2016;43(5):1230–8.
[16] Herrmann KH, Kramer M, Reichenbach JR. Time efficient 3D radial UTE sampling with fully automatic delay compensation on a clinical 3T MR scanner. PLoS One 2016;11(3):e0150371.
[17] Allen-Auerbach M, Yeom K, Park J, Phelps M, Czernin J. Standard PET/CT of the chest during shallow breathing is inadequate for comprehensive staging of lung cancer. J Nucl Med 2006;47(2):298–301.
[18] Feng L, Delacoste J, Smith D, Weissbrot J, Flagg E, Moore WH, et al. Simultaneous evaluation of lung anatomy and ventilation using 4D respiratory-motion-resolved Ultrashort Echo time sparse MRI. J Magn Reson Imaging 2019;49(2):411–22.
[19] Zhu X, Chan M, Lustig M, Johnson KM, Larson PEZ. Iterative motion-compensation reconstruction ultra-short TE (iMoCo UTE) for high-resolution free-breathing pulmonary MRI. Magn Reson Med 2020;83(4):1208–21.
[20] Peguret N, Ozsahin M, Zeverino M, Belmondo B, Durham AD, Lovis A, et al. Apnea-like suppression of respiratory motion: first evaluation in radiotherapy. Radiother Oncol 2016;118(2):220–6.
[21] Beigelman-Aubry C, Peguret N, Stuber M, Delacoste J, Belmondo B, Lovis A, et al. Chest-MRI under pulsatile flow ventilation: a new promising technique. PLoS One 2017;12(6):e0178807.
[22] Delacoste J, Dournes G, Dunet V, Ogna A, Noirez L, Simons J, et al. Ultrashort echo time imaging of the lungs under high-frequency noninvasive ventilation: a new approach to lung imaging. J Magn Reson Imaging 2019;50(6):1789–97.
[23] Delacoste J, Chaptinel J, Beigelman-Aubry C, Piccini D, Sauty A, Stuber M. A double echo ultra short echo time (UTE) acquisition for respiratory motion-suppressed high resolution imaging of the lung. Magn Reson Med 2018;79(4):2297–305.
[24] Delacoste J, Dournes G, Dunet V, Ogna A, Noirez L, Simons J, et al. Ultrashort echo time imaging of the lungs under high-frequency noninvasive ventilation: a new approach to lung imaging. J Magn Reson Imaging 2019;50(6):1789–97.
[25] Ogna A, Bernasconi M, Belmondo B, Long O, Simons J, Peguret N, et al. Prolonged Apnea supported by high-frequency noninvasive ventilation: a pilot study. Am J Respir Crit Care Med 2017;195(7):958–60.
[26] Nielles-Vallespin S, Weber MA, Bock M, Bongers A, Speier P, Combs SE, et al. 3D radial projection technique with ultrashort echo times for sodium MRI: clinical applications in human brain and skeletal muscle. Magn Reson Med

2007;57(1):74–81.
[27] Piccini D, Littmann A, Nielles-Vallespin S, Zenge MO. Spiral phyllotaxis: the natural way to construct a 3D radial trajectory in MRI. Magn Reson Med 2011;66(4):1049–56.
[28] Mugler JPI, Fielden SW, Meyer CH, Altes TA, Miller GW, Stemmer A, et al. Breath-hold UTE lung imaging using a stack-of-spirals acquisition. Proc Intl Soc Mag Reson Med 2015. Toronto, Canada, #1476.
[29] Fielden S, Mugler J, Miller W, Stemmer A, Pfeuffer J, Kiefer B, et al. A Variable-TE Stack-of-spirals sequence for 3D UTE imaging. Proc Intl Soc Mag Reson Med 2016. Singapore, #1062.
[30] Ma W, Sheikh K, Svenningsen S, Pike D, Guo F, Etemad-Rezai R, et al. Ultra-short echo-time pulmonary MRI: evaluation and reproducibility in COPD subjects with and without bronchiectasis. J Magn Reson Imaging 2015;41(5):1465–74.
[31] Bankier AA, MacMahon H, Goo JM, Rubin GD, Schaefer-Prokop CM, Naidich DP. Recommendations for measuring pulmonary nodules at CT: a statement from the Fleischner society. Radiology 2017;285(2):584–600.
[32] Callister ME, Baldwin DR, Akram AR, Barnard S, Cane P, Draffan J, et al. British Thoracic Society guidelines for the investigation and management of pulmonary nodules. Thorax 2015;70(Suppl. 2):ii1–54.
[33] Oudkerk M, Devaraj A, Vliegenthart R, Henzler T, Prosch H, Heussel CP, et al. European position statement on lung cancer screening. Lancet Oncol 2017;18(12):e754–66.
[34] Grodzki DM, Jakob PM, Heismann B. Ultrashort echo time imaging using pointwise encoding time reduction with radial acquisition (PETRA). Magn Reson Med 2012;67(2):510–8.
[35] Ohno Y, Chen Q, Hatabu H. Oxygen-enhanced magnetic resonance ventilation imaging of lung. Eur J Radiol 2001;37(3):164–71.
[36] Lonzetti L, Zanon M, Pacini GS, Altmayer S, Martins de Oliveira D, Rubin AS, et al. Magnetic resonance imaging of interstitial lung diseases: a state-of-the-art review. Respir Med 2019;155:79–85.
[37] Ohno Y, Koyama H, Yoshikawa T, Nishio M, Matsumoto S, Iwasawa T, et al. Pulmonary magnetic resonance imaging for airway diseases. J Thorac Imaging 2011;26(4):301–16.
[38] Dournes G, Menut F, Macey J, Fayon M, Chateil JF, Salel M, et al. Lung morphology assessment of cystic fibrosis using MRI with ultra-short echo time at submillimeter spatial resolution. Eur Radiol 2016;26(11):3811–20.
[39] Rana P, Sodhi KS, Bhatia A, Saxena AK, Suri D, Singh S. Diagnostic accuracy of 3-T lung magnetic resonance imaging in human immunodeficiency virus-positive children. Pediatr Radiol 2020;50(1):38–45.
[40] Biederer J, Ohno Y, Hatabu H, Schiebler ML, van Beek EJR, Vogel-Claussen J, et al. Screening for lung cancer: does MRI have a role? Eur J Radiol 2017;86:353–60.
[41] Meier-Schroers M, Homsi R, Skowasch D, Buermann J, Zipfel M, Schild HH, et al. Lung cancer screening with MRI: results of the first screening round. J Cancer Res Clin Oncol 2018;144(1):117–25.
[42] De Koning H, Van Der Aalst C, Ten Haaf K, Oudkerk M. PL02.05 effects of volume CT lung cancer screening: mortality results of the NELSON randomised-controlled population based trial. J Thorac Oncol 2018;13(10, Supplement):S185.
[43] Chassagnon G, Martin C, Ben Hassen W, Freche G, Bennani S, Morel B, et al. High-resolution lung MRI with ultrashort-TE: 1.5 or 3 tesla? Magn Reson Imaging 2019;61:97–103.
[44] Campbell-Washburn AE, Ramasawmy R, Restivo MC, Bhattacharya I, Basar B, Herzka DA, et al. Opportunities in interventional and diagnostic imaging by using high-performance low-field-strength MRI. Radiology 2019;293(2):384–93.